

# Coherent postionization dynamics of molecules based on adiabatic strong-field approximation

Shan Xue,<sup>1,2</sup> Wenli Yang,<sup>1,2</sup> Ping Li,<sup>1,2</sup> Yuxuan Zhang,<sup>1,2</sup> Pengji Ding,<sup>1,2,\*</sup> Song-Feng Zhao,<sup>3</sup> Hongchuan Du,<sup>1,2,†</sup> and Anh-Thu Le<sup>4</sup>

<sup>1</sup>Frontiers Science Center for Rare Isotopes, Lanzhou University, Lanzhou 730000, China

<sup>2</sup>School of Nuclear Science and Technology, Lanzhou University, Lanzhou 730000, China

<sup>3</sup>Key Laboratory of Atomic and Molecular Physics and Functional Materials of Gansu Province, College of Physics and Electronic Engineering, Northwest Normal University, Lanzhou 730070, China

<sup>4</sup>Department of Physics, University of Connecticut, Storrs, Connecticut 06268, United States

(Dated: November 21, 2023)

Open-system density matrix methods typically employ incoherent population injection to investigate the postionization dynamics in strong laser fields. The presence of coherence injection has long been a subject of debate. In this context, we introduce a coherence injection model based on the adiabatic strong-field approximation (ASFA). This model effectively predicts ionic coherence resulting from directional tunnel ionization. With increasing field strength, the degree of coherence predicted by the ASFA model gradually deviates from that of the SFA model but remains much milder compared to the results of the simple and partial-wave expansion models. The impact of coherence injection on the postionization molecular dynamics is explored in O<sub>2</sub> and N<sub>2</sub>. We find that the ionization-induced vibrational coherence strongly enhances the population inversion of  $X^2\Sigma_g^+ - B^2\Sigma_u^+$  in N<sub>2</sub><sup>+</sup> and the dissociation probability of O<sub>2</sub><sup>+</sup>. Conversely, the ionization-induced vibronic coherences have inhibitory effects on the related transitions. These findings reveal the significance of including the vibronic-state-resolved coherence injection in simulating molecular dynamics following strong-field ionization.

## I. INTRODUCTION

Strong field ionization of electrons from multiple molecular orbitals (MOs) and the subsequent electric dipole coupling between ionic states result in diverse molecular dynamics [1–4]. This includes the attosecond-scale charge migration and the charge transfer process driven by electron-nuclear interactions occurring on femtosecond to picosecond timescales [4–9]. The observation of such ultrafast dynamics relies on the existence of interstate coherences and is crucial for understanding the electronic and nuclear dynamics taking place upon the strong-field ionization, which could play key roles in chemical and biological reactions.

To theoretically investigate the “postionization” molecular dynamics, one should consider both the multi-electron effect and the nuclear motion. This renders the utilization of the full-dimensional time-dependent Schrödinger equation (TDSE) impractical. Thus far, full-dimensional TDSE calculations for molecules have been constrained to small molecules like H<sub>2</sub> [10, 11]. There have been very few *ab-initio* calculations for more complex molecular systems [12]. To address this issue, an open-system density matrix (DM) method has been developed recently [13–16]. By injecting the reduced DM (RDM), generated upon transient strong-field ionization, into the DM equations, the photoionization, electric dipole coupling and nuclear motion could be treated on

the same foot in principle. So far, current RDM injection methods typically only account for the most intuitive injection of the ionic state populations. The injection of the nondiagonal terms of the instantaneous RDM, i.e., the coherences, is not adequately considered. Despite this simplified assumption, theoretical simulations still qualitatively align with experimental results, leaving the effect of coherence injection uncertain. In fact, strong-field ionization could lead to coherences in the ion ensemble. The electronic coherence produced by photoionization has been studied extensively in atomic systems in both the linear and nonlinear regimes [17–20]. The situation becomes more complex when considering the nuclear motion. After photoionization, the ionic coherences typically decay in a few to hundreds of femtoseconds due to the dephasing and overlap decrease of the nuclear wavepacket [12, 21, 22]. Such nuclear-motion-induced coherence evolution should be properly included when investigating molecular dynamics.

Based the strong-field approximation (SFA), Pabst *et al.* proposed an intuitive coherence injection model, which successfully explained the ionization-induced coherence in atom xenon [19]. We further extend this model to diatomic molecular systems, and its validity has been verified on a one-dimensional H<sub>2</sub> system [23]. Recently, this coherence model has been used to explain the abnormal ellipticity dependence of N<sub>2</sub><sup>+</sup> lasing [24]. Due to its intuitiveness, we refer to it as the simple model in this work. However, it may overestimate the ionic state coherence generated upon tunnelling ionization. Recently, Yuen *et al.* developed an alternative coherence model using the partial wave expansion (PWE) approach [25]. At the lowest order of the weak field asymptotic theory,

\* dingpj@lzu.edu.cn

† duhch@lzu.edu.cn

the partial wave ionization amplitudes are calculated, enabling the synthesis of the ionic RDM. This model is at the same level of accuracy as the molecular Ammosov-Delone-Krainov (MOADK) theory in terms of calculating the ionization rate. However, according to the exact SFA, ionizations from MOs with opposite symmetries do not yield coherence between the corresponding ionic states. This contradicts the expectations of the simple model and the PWE model. It is this discrepancy that motivated the current research.

In this work, we examine how the adiabatic field-distorted MOs affect the ionization-produced RDM. Adiabatic MOs have previously been employed in the researches on strong-field ionization and high-order harmonic generation of molecules, leading to essential improvements when compared with experimental data [26–28]. For the ionization-induced coherence injection, coupled with the strong-field approximation (SFA), we utilize the distorted orbitals to calculate the transient RDM of the molecular ion. This model is referred to as the adiabatic SFA (ASFA) coherence model. The ASFA model resolves the problem existing in the SFA model, where ionizations from certain MOs do not generate ionic coherence. With increasing electric field strength, the degree of coherence (DOC) predicted by the ASFA model gradually deviates from the results of the SFA model. Taking nuclear vibration into account, the ionization-produced coherence can be divided into the vibrational coherence and vibrational-electronic (vibronic) coherence. We found that these two types of coherence play entirely different roles in influencing the transition direction.

The paper is structured as follows. In Sec. II, we provide a brief review of the simple and PWE coherence models and introduce the (A)SFA coherence model. In Sec. III, using  $N_2$  and  $O_2$  as illustrative examples, we compare the results from different models and investigate the impact of coherence injection on the post-ionization dynamics. Section IV provides a summary. Atomic units are used throughout unless indicated otherwise.

## II. THEORETICAL MODEL

In this section, several coherence injection models are reviewed and introduced, including the simple coherence model, PWE coherence model, SFA and ASFA coherence models. These models are then coupled with the optical Bloch equations to simulate the postionization molecular dynamics.

### A. Simple and partial wave expansion coherence models

After strong-field tunnel ionization, the ionic wave function with  $n$  electron can be approximated using a

single Slater determinant.

$$\Psi(\mathbf{r}_1, \dots, \mathbf{r}_n) = \sum_{i, \mathbf{p}} c_i(\mathbf{p}) \hat{P}_{kn} [\Phi_i(\mathbf{r}_1, \dots, \mathbf{r}_k, \dots, \mathbf{r}_{n-1}) \psi_{\mathbf{p}}(\mathbf{r}_n)] \quad (1)$$

Here,  $\Phi_i$  is the  $i$ -th ionic state, also represented using a single Slater determinant.  $\psi_{\mathbf{p}}$  represent the accompanying continuum state with momentum  $\mathbf{p}$ .  $\hat{P}_{kn}$  is the antisymmetrizing permutation operator on the  $k$ -th and  $n$ -th electron coordinates [29].  $c_i(\mathbf{p})$  characterizes the corresponding ionization amplitude from the neutral to the ionic state. In the basis of ionic eigenstates, the ionic RDM element can be calculated by tracing out the free electrons and reads  $\rho_{ij} = \sum_{\mathbf{p}} c_i(\mathbf{p}) c_j^*(\mathbf{p})$ . For strong-field ionization under an instantaneous electric field  $F$ , the ionization amplitude is field-strength dependent and the RDM is denoted as  $\rho_{ij}^{\text{ins}}(F)$ . Its diagonal terms represent the ionization rates to different ionic states, and the off-diagonal terms signify the ionization-induced coherences.

In the simple model, one assumes that the electron wave packets tunnelling out from different ionization MOs are identical except a constant phase of  $\phi$ , then the Cauchy-Schwarz inequality can be applied

$$\rho_{ij}^{\text{ins(Simple)}} = \sqrt{\sum_{\mathbf{p}} |c_i(\mathbf{p})|^2 \sum_{\mathbf{p}} |c_j^*(\mathbf{p})|^2} \times e^{i\phi}. \quad (2)$$

The diagonal elements still accurately represent the ionization rates, typically replaced by the MOADK rate  $\Gamma_i(F)$  [30, 31], while the off-diagonal elements are considerably overestimated. To determine the ionization phase  $\phi$ , we undertake a straightforward derivation. Considering a positive electric field  $F$  along the  $z$  direction, electrons predominantly ionize in the negative direction with the most probable momentum of  $-p$ . The ionization amplitude can be approximated as  $c_i(-p; F) \approx u_i(-p)F$ . Conversely, for a negative electric field  $-F$ , the ionization amplitude reads  $c_i(p; -F) \approx -u_i(p)F$ . Here,  $u_i(p) \sim -\int \varphi_i(r) z e^{-ipz} dr$ , representing the ionization transition dipole moment (TDM) with  $\varphi_i$  as the ionization Dyson orbital. For homonuclear diatomic molecules, the MOs exhibit well-defined symmetries, either  $g$  or  $u$ . It can be inferred that for a  $g$  orbital,  $c_i(F) = c_i(-F)$ , while for a  $u$  orbital,  $c_i(F) = -c_i(-F)$ . Therefore, when two ionization orbitals possess the same symmetries,  $\rho_{ij}(F) = \rho_{ij}(-F)$ . When they possess opposite symmetries,  $\rho_{ij}(F) = -\rho_{ij}(-F)$ . In simpler terms, an intuitive way to define the exponential term in Eq. (2) could be  $\text{sgn}[F]^{(2-P_i-P_j)/2}$ . Here,  $\text{sgn}$  is the sign function, and  $P_{i(j)}$  describes the inversion symmetry of the ionization orbital, with a value of  $+/-1$  representing the  $g/u$  symmetry. Finally, in the simple coherence model, the instantaneous RDM can be expressed as

$$\rho_{ij}^{\text{ins(Simple)}} = \sqrt{\Gamma_i \Gamma_j} \text{sgn}[F(t)]^{(2-P_i-P_j)/2} \quad (3)$$

This equation is exactly the one developed in Ref. [[19]] and has been extended to molecular systems, applied

within the framework of the strong-field transient ionization model [24].

Recently, Yuen *et al.* proposed an alternative coherence model [25]. Based on the PWE and weak field asymptotic theory [32, 33], the instantaneous RDM element is expressed as

$$\rho_{ij}^{\text{ins(PWE)}} = \sum_m \gamma_{im}(F) \gamma_{jm}^*(F) \quad (4)$$

where  $\gamma_{im}$  is the partial ionization amplitude with  $m$  being the magnetic quantum number. Using the adiabatic approximation, one identifies  $\gamma_{im}$  as

$$\begin{aligned} \gamma_{im} = & \frac{B_{im}}{\sqrt{2^{|m|}|m|!} \kappa_i^{Z/\kappa_i - 1/2}} \left( \frac{2\kappa_i^3}{|F(t)|} \right)^{Z/\kappa_i - (|m|+1)/2} \\ & \times \exp \left[ \frac{-\kappa_i^3}{3|F(t)|} + \frac{i\pi}{4} + i\pi \left( \frac{Z}{\kappa_i} - \frac{|m|+1}{2} \right) \right] \end{aligned} \quad (5)$$

where  $\kappa_i = \sqrt{2E_i}$  with  $E_i$  being the binding energy and  $Z$  being the effective charge after ionization. Taking into account that the electrons turned to be ionized in the opposite direction to the electric field,  $B_{im}$  takes the form

$$B_{im} = \begin{cases} \sum_{l, m_0} C_{i, lm_0} D_{mm_0}^l(\alpha, \beta, \gamma) Q(l, m) & F < 0 \\ \sum_{l, m_0} (-1)^{l-m_0} C_{i, lm_0} D_{mm_0}^l(\alpha, \beta, \gamma) Q(l, m) & F > 0 \end{cases} \quad (6)$$

where

$$Q(l, m) = (-1)^{(m+|m|)/2} \sqrt{(2l+1)(l+|m|)!/2(l-|m|)!} \quad (7)$$

Here,  $l$  is the orbital angular momentum quantum number.  $m, m_0$  are the magnetic quantum number along the space  $z$ -axis and molecule axis, respectively.  $D_{mm_0}^l$  represents the Wigner D-matrix for rotating the molecule.  $C_{i, lm_0}$  is the structure parameter of the MO ionized to the  $i$ -th ionic state [31]. It is noteworthy that this model is consistent with the MOADK theory in terms of ionization rates, enabling the calculation of the tunnel ionization rates of molecules at different angles.

## B. Adiabatic strong-field approximation coherence model

In this section, we introduce the coherence model based on the ASFA theory. The adiabatic field-distorted MOs are utilized for the calculation of the instantaneous RDM. In the length-gauge SFA, the amplitude for creating an ion in the  $i$ -th state accompanied by a free electron with canonical momentum  $\mathbf{k}$  at the end of the laser field  $t_f$  reads

$$M_i(\mathbf{k}, t_f) = i \int_{-\infty}^{t_f} \mathbf{u}_i(\mathbf{p}) \cdot \mathbf{F}(t) e^{-i \int_t^{t_f} |\mathbf{p}|^2/2 - E_i dt'} dt \quad (8)$$

Here,  $\mathbf{u}_i(\mathbf{p}) = \langle \psi_{\mathbf{p}} | r | \varphi_i \rangle$  is the ionization TDM.  $\varphi_i$  is the ionization Dyson orbital, which is approximated by the neutral MO in this work.  $E_i$  is the corresponding binding

energy.  $\mathbf{p} = \mathbf{k} + \mathbf{A}(t)$  is the kinetic momentum with  $\mathbf{A}$  being the field vibronic coherence vector potential. In the adiabatic tunnelling regime, the laser field at the ionization instant can be treated as a static electric field, causing the distortion of MOs under its influence. Then the MO is the eigenfunction of the field-dependent Hamiltonian operator.

$$\hat{f}(t) |\varphi_i\rangle = E_i |\varphi_i\rangle \quad (9)$$

with  $\hat{f}(t)$  is a combination of the field-free Hamiltonian operator  $\hat{f}_0$  and the term  $\mathbf{F}(t) \cdot \mathbf{r}$  describing the interaction with the instantaneous electric field. Now the eigenenergy  $E_i$  is field dependent. In this study, adiabatic MOs are computed using the density-functional theory as implemented in the GAUSSIAN16 program package [34]. The B3LYP correlation-exchange functional and the augmented correlation-consistent polarized valence quadruple-zeta (aug-cc-pVTZ) basis set are employed. The basis set incorporates diffuse functions to accurately represent the field-induced wave function diffusion.

Tracing out the degree of freedom of the ionized electron produces the RDM of the ion ensemble

$$\rho_{ij}(t_f) = \int d\mathbf{k} M_i(\mathbf{k}, t_f) M_j^*(\mathbf{k}, t_f). \quad (10)$$

Assuming that electron wavepackets contributing to the same  $\mathbf{k}$  but emitted at different times have negligible overlap due to rapid wavepacket spreading, the coherence can be determined by neglecting the terms where two ionic states are populated at different times. Consequently, Eq. (10) simplifies to

$$\begin{aligned} \rho_{ij}(t_f) = & \int_{-\infty}^{t_f} \rho_{ij}^{\text{ins}}(t) e^{i(E_i - E_j)(t_f - t)} dt \\ = & \int_{-\infty}^{t_f} \left( \int [\mathbf{u}_i(\mathbf{p}) \cdot \mathbf{F}(t)] [\mathbf{u}_j(\mathbf{p}) \cdot \mathbf{F}(t)] d\mathbf{p} \right) e^{i(E_i - E_j)(t_f - t)} dt. \end{aligned} \quad (11)$$

The equation above represents the RDM that the ion ensemble can attain after the pulse is over, which is the original form of the coherence model in Ref. [19].  $\rho_{ij}^{\text{ins}}$  is the transient injected RDM at each ionization instant.

To be noted, equation (11) does not consider the dipole coupling among the ionic states during the laser-molecule interaction. To incorporate the coupling effect,  $\rho_{ij}^{\text{ins}}$  needs to be injected into the optical Bloch equation, as detailed in Eq. (13) in the subsequent section. However,  $\rho_{ij}^{\text{ins}}$  fails to provide ionization rates (diagonal terms) with appropriate magnitudes. To achieve a more realistic injected DM, the diagonal terms are replaced by the MOADK rate  $\Gamma_{i(j)}$ . While maintaining the DOC unchanged, the coherences are now expressed as  $G^{(A)} \sqrt{\Gamma_i \Gamma_j}$ .  $G^{(A)}$  is defined as a complex DOC,

$$G_{ij}^{(A)} = \rho_{ij}^{\text{ins}} / \sqrt{\rho_{ii}^{\text{ins}} \rho_{jj}^{\text{ins}}}. \quad (12)$$

which characterize both the DOC and the phase of coherence predicted by different models. The revised instantaneous DM is now denoted as  $\rho_{ij}^{\text{ins(A)}}$ . The superscript ‘‘A’’ can be either ‘‘SFA’’ or ‘‘ASFA’’, depending

on whether the MOs adopted are field-free or adiabatic field-distorted, respectively. The complex DOC is also used for the simple and PWE models with A=Simple or PWE.

### C. Optical Bloch equations

At this stage, we are equipped to employ the coherence models for calculating the instantaneous RDM produced upon the strong-field ionization. By incorporating it into the optical Bloch equations, one can simulate the evolution of the ionic system. For molecules interacting with electric fields within tens of femtoseconds, the DM can be expanded in terms of the vibronic states under the Born-Oppenheimer (BO) approximation,  $\rho_{vv'}^{ij} = \langle \Phi_i \chi_v^i | \hat{\rho} | \Phi_j \chi_{v'}^j \rangle$ , where  $\Phi_i$  and  $\chi_v^i$  represent the  $i$ -th electronic state and  $v$ -th vibrational state on the  $i$ -th ionic potential energy curve. Then the optical Bloch equations read

$$i \frac{\partial}{\partial t} \rho_{vv'}^{ij} = \omega_{vv'}^{ij} \rho_{vv'}^{ij} - \mathbf{F}^{(\text{MF})} \cdot \sum_{o,v''} (\mathbf{u}_{vv''}^{io} \rho_{v''v'}^{oj} - \rho_{vv''}^{io} \mathbf{u}_{v''v'}^{oj}) + i \Gamma_{vv'}^{ij}, \quad (13)$$

where  $\omega_{vv'}^{ij} = E_v^i - E_{v'}^j$  is the energy difference between vibronic states.  $\mathbf{u}_{vv'}^{ij} = \langle \chi_v^i | \mathbf{u}_{ij}(R) | \chi_{v'}^j \rangle$  is the vibronic-state TDM with  $\mathbf{u}_{ij} = -\langle \psi_i | \mathbf{r} | \psi_j \rangle$  being the  $R$ -dependent electronic-state TDM.  $\mathbf{F}^{(\text{MF})}$  is the electric field defined in the molecule-fixed (MF) coordinate system, which can be transformed from the electric field in the space-fixed (SF) coordinate system  $\mathbf{F}^{(\text{SF})}$  by  $\mathbf{F}^{(\text{MF})} = \mathbf{R}(\alpha, \beta, \gamma) \mathbf{F}^{(\text{SF})}$  [24]. Here,  $\alpha$ ,  $\beta$  and  $\gamma$  are the Euler angles in the  $zyz$  convention.  $\mathbf{R}$  is the rotational matrix.

The term  $\Gamma_{vv'}^{ij}(t)$  represents the transient RDM elements injected at each ionization instant, which reads

$$\Gamma_{vv'}^{ij}(t) = \rho_{iv,jv'}^{\text{ins(A)}} C_v^{i(\text{FC})} C_{v'}^{j(\text{FC})} \times n(t). \quad (14)$$

$C_v^{i(\text{FC})} = \langle \chi_v^i | \chi_0^{(\text{neutral})} \rangle$ , where  $\chi_0^{(\text{neutral})}$  represents the vibrational ground state of the neutral molecule. The square of  $C_v^{i(\text{FC})}$  is the Franck-Condon factor from  $\chi_0^{(\text{neutral})}$  to  $\chi_v^i$ .  $n(t)$  accounts for the remaining population probability of the neutral state at time  $t$ . The superscript ‘‘A’’ represents different coherence models with A=Simple, PWE, SFA, or ASFA. In the vibronic-state basis, two types of coherence can be distinguished. When  $i = j$ ,  $\Gamma_{vv}^{ii}$  is referred to as the vibrational coherence (VC). When  $i \neq j$ ,  $\Gamma_{vv'}^{ij}$  is known as the vibronic coherence (VEC). In Sec. III, we will discuss the impact of injecting these two types of coherence on molecular dynamics.

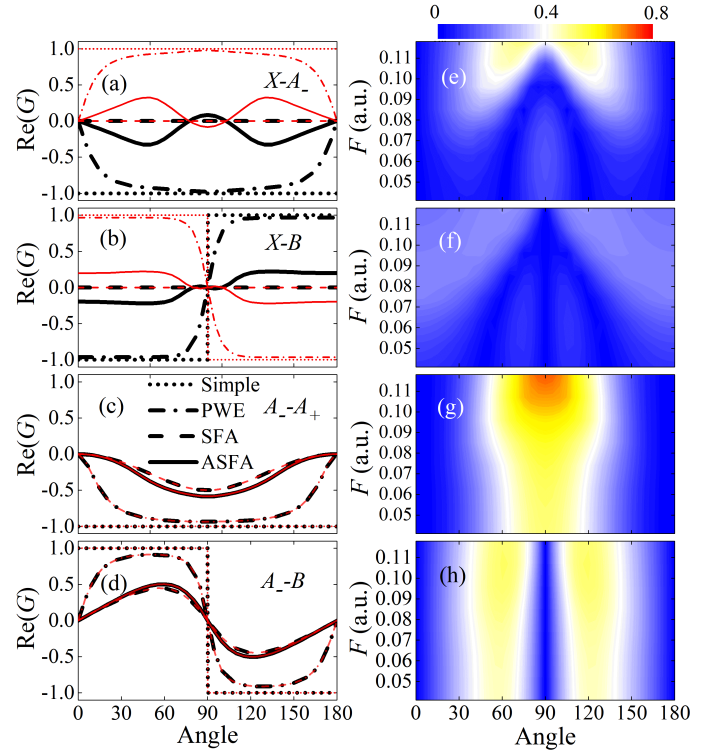


FIG. 1. (Color online) (a)-(d) Real components of the complex degree of coherence for  $X - A_-$ ,  $X - B$ ,  $A_- - A_+$  and  $A_- - B$  at  $F = 0.09$  a.u. (Black thick lines) and  $F = -0.09$  a.u. (Red thin lines), respectively. (e)-(h) Field-strength-dependent degree of coherence for  $X - A_-$ ,  $X - B$ ,  $A_- - A_+$  and  $A_- - B$  calculated by the ASFA model, respectively.

## III. RESULTS AND DISCUSSION

In the following sections, we will begin by using  $\text{N}_2$  as an illustrative target to investigate the influence of coherence injection on the postionization dynamics, with a focus on the  $\text{N}_2^+$  population inversion, which is closely related to the mechanism of  $\text{N}_2^+$  lasing [35–40]. We will then extend our analysis to  $\text{O}_2$  to gain further insights into the influence of coherence injection on the dissociative ionization dynamics.

### A. Coherence injection in the postionization dynamics of $\text{N}_2$

When an intense laser interacts with  $\text{N}_2$ , strong-field ionization of one electron results in the formation of  $\text{N}_2^+$ . This process primarily populates four ionic states that are strongly coupled under the influence of the electric field. Ionizations from the highest occupied molecular orbital (HOMO,  $3\sigma_g$ ), HOMO-1 ( $1\pi_{u\pm}$ ) and HOMO-2 ( $2\sigma_u$ ) produce ionic states  $X^2\Sigma_g^+$ ,  $A^2\Pi_{u\mp}$  and  $B^2\Sigma_u^+$ , abbreviated as  $X$ ,  $A\mp$  and  $B$  for simplicity. The degenerate  $\pi$  orbitals are defined using a spherical basis, with

$\pi_{\pm} = (\mp\pi_x - i\pi_y)/\sqrt{2}$ . According to the orbital symmetries, there are the parallel transition of  $X - B$  and the perpendicular transition of  $X - A_{\mp}$ . The perpendicular TDM element reads  $u_{XA_{\mp}} = -\langle 1\pi_{u_{\pm}}|\mathbf{r}|3\sigma_g\rangle = (\mp u_x \mathbf{e}_x + i u_y \mathbf{e}_y)/\sqrt{2}$ , where  $u_{x(y)} = -\langle 1\pi_{x(y)}|x(y)|3\sigma_g\rangle$ .

Let's start by examining the complex DOC ( $G_{ij}$ ) produced upon strong-field ionization. In Figs. 1(a)-1(d), the angle-dependent behavior of  $G_{ij}$  predicted by different coherence models are depicted, with a fixed field strength of  $F = \pm 0.09$  a.u. Notably, only the PWE model introduces a slight imaginary component of  $G_{ij}$ , while other models provide only real components (see Figs. 7(i-l) and the analysis). Thus, only the real parts of  $G_{ij}$  are depicted. Analyzing the figures reveals three key features. (i) Except for the SFA model, all models predict the existence of the  $X - A_{\pm}$  and  $X - B$  coherences upon strong-field ionization. (ii) Across most angles, the coherence trends consistently exhibit phase similarities for these models. When the field direction reverses, all models produce identical phase jump outcomes, namely

$$\begin{aligned} G_{XA_{-}}(F) &= -G_{XA_{-}}(-F) \\ G_{XB}(F) &= -G_{XB}(-F) \\ G_{A_{-}A_{+}}(F) &= G_{A_{-}A_{+}}(-F) \\ G_{A_{-}B}(F) &= G_{A_{-}B}(-F). \end{aligned}$$

In Figs. 1(a) and 1(d), only the DOC related to  $A_{-}$  is presented. For the another degenerate state  $A_{+}$ ,  $G_{XA_{+}} = -G_{XA_{-}}$  and  $G_{A_{+}B} = -G_{A_{-}B}$ . (iii) The simple model yields the highest DOC, followed by the PWE model. In contrast, the SFA and ASFA models predict much lower DOCs. This is because the latter models consider ionization TDMs to the continuum state from all directions. After tracing out these free electrons, the DOC is considerably reduced compared to that of the PWE model. Moreover,  $G_{XA_{-}}^{\text{(ASFA)}}$  exhibits a dip structure around  $60^{\circ} \sim 120^{\circ}$ . Further analysis indicates that this can be attributed to the abnormal shape of the distorted ionization orbital  $3\sigma_g$  (see Figs. 7(a-d) in the Appendix).

We further examine how the DOC changes with the field strength. According to Eq. (3), the transient DOC predicted by the simple model remains constant with laser intensity. The same holds for the SFA model since the ionization MOs remain unaffected by the field. In the case of the PWE model, the predicted DOCs exhibit subtle decreases as the field strength increases (less than 5% within  $F \in 0.04 \sim 0.12$  a.u.). This negligible change is due to the fact that the phase in Eq. (5) does not depend on  $F$ . In contrast, the ASFA model predicts a notable increase of DOC with increasing field strength, as illustrated in Figs. 1(e-h). At low field strengths, the DOCs of  $X - A_{\pm}$  and  $X - B$  approach zero, resembling the results of the SFA model with field-free MOs. As the field strength increases, their DOCs gradually emerge but remain lower than those of  $A_{+} - A_{-}$  and  $A_{\pm} - B$ . It appears that the coherences of  $X - A_{\pm}$  and  $X - B$  are more susceptible to orbital distortions.

The DOC variations with field strength depicted in

Figs. 1(e-h) align with the transition of the ionization mechanisms. With increasing laser intensity, the strong-field ionization gradually shifts from the multiphoton regime to the tunnelling regime. At low intensities, the orbitals undergo negligible distortions. The MOs almost have well-defined symmetries of  $g/u$ . Remembering  $\mathbf{u}_i(\mathbf{p}) \sim -\int \varphi_i \mathbf{r} e^{-i\mathbf{p}\mathbf{r}} d\mathbf{r}$ ,  $\mathbf{u}_i(\mathbf{p})$  should be purely imaginary/real and possesses  $u/g$  symmetry for a  $g/u$  MO. According to Eq. (11), the instantaneous coherence generated by orbitals with opposite symmetries is zero. This is exactly the case for the  $X - A$  and  $X - B$  state pairs. In the multiphoton regime, the ionization-induced coherence primarily depends on the parities of the ionization MOs. The results from the SFA and ASFA models should be similar (see Figs. 3(a) and 3(b)). With increasing intensity, directional tunnelling ionization disrupts the orbital parity. This results in electrons ionized from different MOs with momentum  $p$  having a certain probability of sharing the same parity. Tracing out these electrons gives rise to the ionization-induced coherence. Moreover, considering that  $c_i(\mathbf{p}) = u_i(\mathbf{p}) \cdot \mathbf{F}$  and  $c_i(\mathbf{p}) = c_i^*(-\mathbf{p})$ , the injected coherence  $\rho_{ij} = \sum_{\mathbf{p}} c_i(\mathbf{p}) c_j^*(\mathbf{p})$  should be a real number. A detailed analysis of the phase of the injected coherence generated by distorted MOs is provided in the Appendix. In general, the ASFA coherence model can be applied to all regimes spanning from multiphoton to tunnelling ionization. In contrast, the simple and PWE models are only applicable to the tunnelling regime and may overestimate the DOC at low laser intensity with Keldysh parameter  $\gamma \sim 1$ .

Next, we explore the impact of coherence injection on the postionization dynamics of  $\text{N}_2$ . In our simulations, a linearly polarized 30-fs laser pulse with an intensity of  $3 \times 10^{14} \text{W/cm}^2$  is employed. Using different coherence models, we calculate the vibronic-state populations of  $\text{N}_2^+$ . Figure 2 shows the populations of  $\chi_0^X$ ,  $\chi_1^X$ ,  $\chi_0^A$ , and  $\chi_0^B$  as functions of the angle at the end of the laser pulse. These vibronic states are chosen due to their close relation to  $\text{N}_2^+$  lasing at 391 nm and 428 nm. It's important to note that, in all four models, the transient vibrational DOCs are nearly identical and approach 100%. Only the vibronic DOCs exhibit significant differences. Comparing the "VC" and "W/O" results, we observe that at small angles,  $\rho_{11}^{XX}$  decreases dramatically, while the population of  $\rho_{00}^{BB}$  increases by about 25%, resulting in a substantial enhancement of the population inversion between  $\chi_{0(1)}^X$  and  $\chi_0^B$  (see Figs. 3(a) and 3(b)).

To understand how the VC injection affects population evolutions, we employ a three-state  $\Lambda$  (or V)-type model for analysis. States 1 and 3 are close in energy and have TDMs to state 2. The optical Bloch equations for this three-state system are as follows,

$$\begin{aligned} \dot{\rho}_{22} &= -2u_{12}F(t)\text{Im}[\rho_{12}] - 2u_{32}F(t)\text{Im}[\rho_{32}] \\ \dot{\rho}_{12} &= -i\omega_{12}\rho_{12} + iu_{12}F(t)(\rho_{22} - \rho_{11}) - iu_{23}F(t)\rho_{13} \\ \dot{\rho}_{32} &= -i\omega_{32}\rho_{32} + iu_{32}F(t)(\rho_{22} - \rho_{33}) - iu_{12}F(t)\rho_{13}^* \\ &\dots \end{aligned} \quad (15)$$

If instantaneous coherence  $\rho_{13}^{\text{ins}}$  is injected at  $t - \delta t$ , the

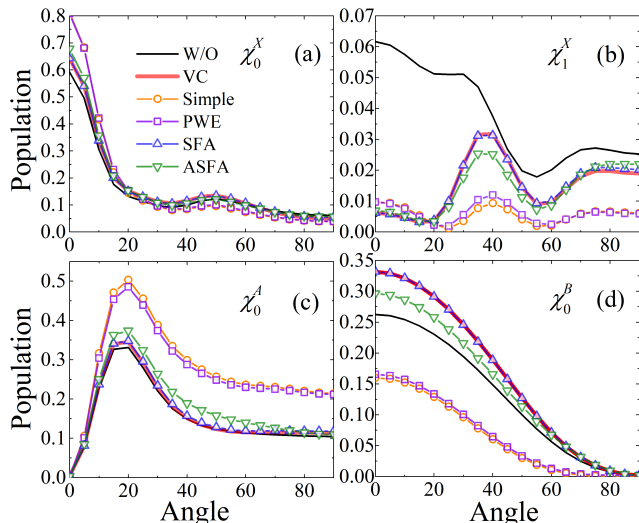


FIG. 2. (Color online) (a)-(d) Populations of  $\chi_0^X$ ,  $\chi_1^X$ ,  $\chi_0^A$  and  $\chi_0^B$  as functions of angle when the laser field is over calculated by different coherence models. “W/O” represents the results calculated without considering coherence injection. “VC” represents the results calculated solely with consideration of the vibrational coherence. The results of  $90^\circ - 180^\circ$  are mirror symmetric to those of  $0^\circ - 90^\circ$  and are not displayed in the figure.

coherence-injection-induced derivative of  $\rho_{22}$  at time  $t$  should be

$$\dot{\rho}_{22}^{\text{VC}}(t) \approx 4u_{32}u_{12}F^2(t)\delta t \text{Re}[\rho_{13}^{\text{ins}}(t - \delta t)]. \quad (16)$$

This simple equation indicates that if  $u_{32}u_{12} \times \text{Re}[\rho_{13}^{\text{ins}}]$  is positive,  $\rho_{13}^{\text{ins}}$  will lead to an increase of  $\rho_{22}$ . This phenomenon can be understood as a constructive interference of the transition amplitudes for the  $1 \rightarrow 2$  and  $3 \rightarrow 2$  paths. For  $N_2^+$ , the vibrational coherence  $\Gamma_{vv'}^{ii}$  is analogous to  $\rho_{13}^{\text{ins}}$  in the three-state system. If  $u_{vv''}^{ik}u_{v''v'}^{ik} \times \Gamma_{vv'}^{ii}$  is positive, the VC injection will enhance the transitions from the two neighboring vibrational states  $\chi_v^i$  and  $\chi_{v'}^i$  to the state  $\chi_{v''}^k$ . Notably, this condition is commonly met in molecules. For example,  $u_{00}^{XB}u_{10}^{XB} \times \Gamma_{01}^{XX} > 0$ , leading to a significant enhancement of  $\rho_{00}^{BB}$  as shown in Fig. 2(d).

To assess the effects of the VEC injection, one should compare the results of the coherence models (lines with symbols) with the “VC” ones (solid thick lines) in Fig. 2. Several features can be concluded. (i) The results of the SFA model closely overlap with the “VC” results, because the SFA model cannot provide coherences of  $X - A_\pm$  and  $X - B$  (see Figs. 1(a) and 1(b)). (ii) When considering the VEC injection, except for the abnormal ASFA-model results around  $90^\circ$ , the simple, PWE, and ASFA models show a consistent trend in the direction of population transfer. For  $\chi_0^X$  and  $\chi_1^X$ , the VEC injection leads to population increases at small angles but population decreases at large angles. For  $\chi_0^A$ , the population increases at all angles for the simple and PWE models and most

angles for the ASFA case. For  $\chi_0^B$ , the population decreases at all angles. The abnormal results around  $90^\circ$  in the ASFA model are due to the dip structure of the  $X - A_\pm$  and  $X - B$  coherences predicted by the ASFA model (see Figs. 1(a) and 1(b)). (iii) Regarding the impact of the VEC injection on the population transfer, the simple model shows the largest magnitude, followed by the PWE model, while the ASFA model yields the smallest magnitude. The reason can be readily seen from Fig. 1, where the simple model predicts the largest VEC, the PWE model is intermediate, and the ASFA model gives a smaller VEC.

This effect of VEC injection can be comprehended by employing a two-state model interacting with an electric field  $F(t) = F_0 \cos(\omega t + \phi)$ . Under rotating wave approximation, the two-state optical Bloch equations read

$$\begin{aligned} \dot{\tilde{\rho}}_{12} &= iu_{12} \frac{F_0}{2} e^{-i\epsilon t + i\phi} \Delta + \tilde{\rho}_{12}^{\text{ins}} e^{-i\omega_{21}t} \\ \dot{\Delta} &= -2u_{12}F_0 \text{Im}(\tilde{\rho}_{12} e^{i\epsilon t - i\phi}), \end{aligned} \quad (17)$$

where  $\Delta = \rho_{22} - \rho_{11}$ ,  $\rho_{12} = \tilde{\rho}_{12} e^{-i\omega_{12}t}$  and  $\epsilon = \omega_{21} - \omega$ . Because  $\tilde{\rho}_{12}(t) = \tilde{\rho}_{12}(t - \delta t) + \tilde{\rho}_{12}^{\text{ins}}(t - \delta t) e^{-i\omega_{21}(t - \delta t)} \delta t + O(\Delta)$ , the population transfer caused directly by coherence injection can be expressed as

$$\Delta^{\text{VEC}} = -2u_{12}F_0 \sin(\epsilon \delta t) \int \text{Re}[\tilde{\rho}_{12}^{\text{ins}}(t)] \cos(\omega t + \phi) dt, \quad (18)$$

In the derivation, it is assumed that the vibronic coherence term is primarily real (see Fig. 1). According to this equation, the direction of the coherence-injection-induced transition depends on the sign of  $u_{12}$  and the integral term. In the case of  $N_2^+$  states,  $\rho_{XA_+}^{\text{ins}}$  and  $\rho_{XB}^{\text{ins}}$  have opposite signs to the electric field (see Fig. 1), so the integration term is smaller than 0. Taking  $\chi_0^X - \chi_0^B$  and  $\chi_1^X - \chi_0^B$  as examples,  $\epsilon$  is positive,  $u_{00}^{XB}$  and  $u_{10}^{XB}$  are negative, so that  $\Delta^{\text{VEC}}$  is negative. This means that the VEC injection has a suppressive effect on the transition from  $\chi_{0(1)}^X$  to  $\chi_0^B$ , resulting in the increase of  $\rho_{00(11)}^{XX}$  and decrease of  $\rho_{00}^{BB}$  compared to that of the “VC” case at small angles. At large angles, the  $X - A$  perpendicular transition dominates. Since  $\omega_{AX} \approx \omega$ ,  $\omega_{v''v}^{AX} - \omega$  can be either positive or negative, leading to different effects of the VEC injection on the vibronic transition from  $X$  to  $A$ . Taking  $\chi_0^X - \chi_0^{A+}$  as an example,  $u_{00(x)}^{XA+} = u_x / \sqrt{2} = -0.125 < 0$  and  $\epsilon < 0$ , so that  $\Delta^{\text{VEC}} > 0$ , leading to a population transfer from  $\chi_0^X$  to  $\chi_0^A$  with VEC injection. Overall, the VEC injection leads to a slight population decrease of  $\chi_{0(1)}^X$  and a population increase of  $\chi_0^A$  at the large angle. After thorough examinations, it is found that Eq. (18) effectively describes the population transfer direction when considering the VEC injection. The impact of VEC injection can also be comprehended from another perspective. Under the influence of an alternating electric field, the ionic electron cloud moves in either a nearly adiabatic or nonadiabatic manner, depending on the value of  $\omega_{21} - \omega$ . Meanwhile,

the transiently injected ion exhibits an electron distribution oriented opposite to the field direction. Due to the Coulomb force, the newly injected electron cloud inevitably influences the movement of the original electron cloud, resulting in either enhancement or suppression of the transition strength in the original direction.

Compared to the population of individual state, people are more interested in the population inversion of  $N_2^+$ , which is related to the lasing generation in ambient air. Figures. 3(a) and 3(b) display the population inversion of  $\chi_{0(1)}^X - \chi_0^B$  with varying laser intensities after angle integration. In the integration, only the angles with population inversion at the end of the pulse are considered. For all intensities, the inversions are enhanced when the VC injection is considered, whereas the VEC injection has a suppressing effect on the inversion. As depicted in Fig. 1, both the PWE and the simple models predict strong vibronic DOCs. This results in a substantial decrease of the population inversions compared to the “VC” case. For the SFA model,  $X - B$  coherence can not be generated. Its results almost overlap with the “VC” ones. With weak vibronic DOC, the ASFA model predicts a population inversion slightly smaller than the “VC” ones. Overall, using the ASFA model, coherence injection will promote the population inversion between  $\chi_{0(1)}^X$  and  $\chi_0^B$ .

To compare the population inversion generated by different models, Figs. 3(c) and 3(d) present the angular distributions at a laser intensity of  $3 \times 10^{14} \text{W/cm}^2$ . At this intensity, predictions from the simple and PWE models significantly deviate from those of other models. While these two models exhibit minimal inversion between  $\chi_0^X$  and  $\chi_0^B$ , specific rotational levels could still achieve population inversion when considering molecular rotation, leading to the lasing amplification [41–43]. As a result, these two models predict that the 391-nm lasing peaks at  $30^\circ$  and  $90^\circ$ , whereas other models predict that the 391-nm lasing peaks at a small angle, and the intensity decreases as the angle increases. These distinctions offer a potential approach to test the validities of the simple and PWE coherence models. For the  $\chi_1^X - \chi_0^B$  population inversion, all models predict the 428-nm lasing peaks at  $0^\circ$ . At this point, distinguishing between the (A)SFA coherence model and the incoherent injection model based on the angle-dependent lasing signals seems challenging. More elaborate experimental designs may be required to detect traces of the coherence injection in the postionization dynamics of  $\text{O}_2$ . Fortunately, in our study on  $\text{O}_2$ , we observed that differences between various coherence models can be discerned through the angle-dependent dissociative ionization signals (see Fig. 6 in Sec. IIIB).

### B. Coherence injection in the postionization dynamics of $\text{O}_2$

When a strong laser field interacts with  $\text{O}_2$ , electrons can ionize from the HOMO ( $1\pi_{g\pm}$ ), HOMO-1 ( $1\pi_{u\pm}$ ),

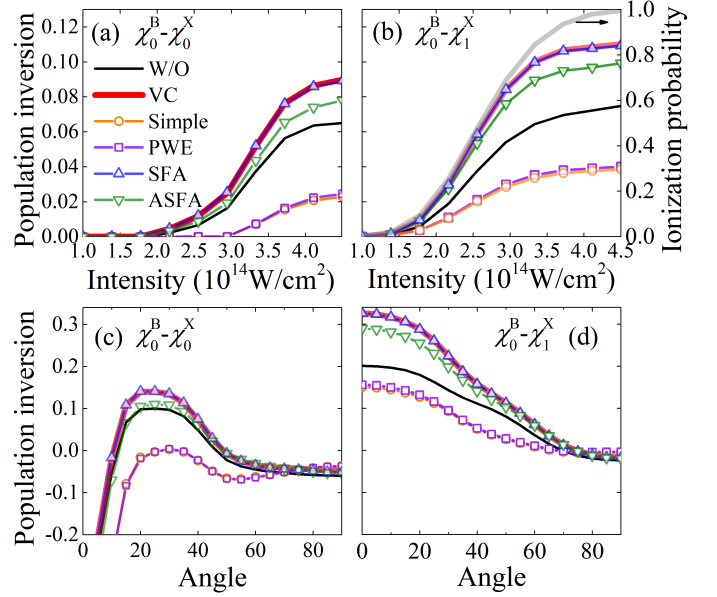


FIG. 3. (Color online) (a), (b) Angle-integrated population inversions of  $\chi_0^X - \chi_0^B$  and  $\chi_1^X - \chi_0^B$  varies with laser intensity at a pulse duration of 30 fs. Only angles with a population inversion greater than 0 are considered in the integration. (c), (d) Angle-dependent population inversion at a laser intensity of  $3 \times 10^{14} \text{W/cm}^2$ .

and HOMO-2 ( $3\sigma_g$ ) orbitals, resulting in the formation of  $\text{O}_2^+$  in the  $X^2\Pi_{g\mp}$ ,  $a^4\Pi_{u\mp}$  and  $b^4\Sigma_g^-$  states, respectively. Previous researches have indicated that  $\text{O}_2^+$  can undergo further dissociation on the  $f^4\Pi_g$  curve by absorbing one photon from state  $a^4\Pi_u$ , generating kinetic energy release (KER) signals in the range of 0 to 2 eV [44–46]. Our previous results verified that the  $b^4\Sigma_g^-$  state also plays a crucial role in the dissociation process through a pathway of  $b^4\Sigma_g^- \rightarrow a^4\Pi_u \rightarrow f^4\Pi_g$  due to the resonant coupling between vibronic states [47]. The  $X^2\Pi_g$  state, however, is subject to a selection rule that prohibits the transition to these three states and is therefore ignored in the calculations. In the following study, we specifically focus on the effects of coherence injection of  $a^4\Pi_u - b^4\Sigma_g^-$  on the dissociation signals. Vibronic states of  $a^4\Pi_{u\pm}$ ,  $b^4\Sigma_g^-$  and  $f^4\Pi_{g\pm}$  are included in the simulation, denoted as  $a_{\pm}$ ,  $b$  and  $f_{\pm}$  for simplicity.

In Figs. 4(a) and 4(b), we calculated the complex DOC  $G_{ij}$  at  $F=0.09$  a.u. with varying angles using different coherence models. Similar to Fig. 1, only the real parts of  $G_{ij}$  are displayed. Two key features can be seen. (i) The trends of coherence provided by several models are generally consistent in phase. Similar to the results for  $\text{N}_2^+$ , the simple model yields the highest DOC, followed by the PWE model. Due to opposite symmetries of  $1\pi_{u\pm}$  and  $3\sigma_g$ , the SFA model cannot generate coherence between  $a_{\mp}$  and  $b$ . However, when considering orbital distortion, the ASFA model can provide the  $a_{\mp} - b$  coherence. The DOC is much smaller compared to

those of the simple and PWE models. This is because Eq. (11) considers the possibility of ionization occurring in all directions. After tracing out the free electrons, the DOC is expected to be less significant. (ii) At small angles, the ASFA model predicts very small coherence which exhibits values opposite to those of the simple and PWE models. This is due to the repulsive behavior between the two spin ( $\uparrow$ ,  $\downarrow$ ) MOs in the unrestricted calculations. The electronic configuration of  $O_2$  reads  $KK(2\sigma_g)^2(2\sigma_u)^2(3\sigma_g)^2(1\pi_{ux})^2(1\pi_{uy})^2(1\pi_{gx})^\uparrow(1\pi_{gy})^\uparrow$ . Each fully occupied orbital can be further divided into  $\uparrow$  and  $\downarrow$  orbitals. Since the spin multiplicities of  $a_\pm$  and  $b$  are 4, the ionization orbitals are  $1\pi_{u\mp}$   $\downarrow$  and  $3\sigma_g$   $\downarrow$ , respectively. Take  $1\pi_{ux}$  as an example, Figs. 4(e) and 4(f) display the  $\uparrow$  and  $\downarrow$  orbitals at  $F = 0.09$  a.u. and  $\beta = 30^\circ$ . Under the influence of the electric field, the  $\uparrow$  orbital tends to distort directly opposite to the field direction. While the  $\downarrow$  orbital experiences not only the field, but also repulsion with the  $\uparrow$  orbital. This leads to the counterintuitive shape of the  $\downarrow$  orbital, resulting in the opposite phase of the  $a_\pm - b$  coherence at  $\sim 30^\circ$  and  $\sim 150^\circ$ .

We also examine the variation of DOC with field strength. Similar to Fig. 1, only the results predicted by the ASFA model are presented in Figs. 4(c) and 4(d), because the DOCs predicted by other models remain nearly constant with varying field strength. As the electric field intensifies, orbital distortion becomes more pronounced, causing the DOC to deviate further from that of the SFA model. The  $a_\pm - b$  DOC gradually strengthens with increasing laser intensity. However, the  $a_+ - a_-$  DOC remains essentially unchanged. These phenomena are consistent with the transitions of the ionization mechanisms from the multiphoton regime to the tunneling regime.

Now, we investigate the impact of transient coherence injection on the dissociative ionization dynamics of  $O_2$ . A linearly polarized 800-nm, 30-fs laser pulse with an intensity of  $1.5 \times 10^{14} \text{W/cm}^2$  is adopted for the simulations on  $O_2$ . At this wavelength, the low vibronic states of  $a_\pm$  and  $b$  experience resonance coupling. In this context, coherence injection will enhance the competition between paths of  $a_\pm \leftrightarrow b$  and  $a_\pm \rightarrow f_\pm$ , leading to substantial changes in the results. Figure 5(a) shows the dissociation probabilities as a function of angle, calculated by different coherence models. First, let's compare the results without coherence injection (W/O, solid thin line) and with VC injection (VC, solid thick line). At small angles, the  $a_\pm \rightarrow f_\pm$  parallel transition dominates. As discussed in Sec. III A using a three-state model (see Eq. (16)), the VC injection on  $a_\pm$  will enhance the dipole transitions from  $a_\pm$  to  $f_\pm$ , resulting in the enhancement of the dissociation probability. While, as the angle increases, the  $a^4\Pi_{u\pm} \rightarrow b^4\Sigma_g^-$  perpendicular transition gradually gains strength. The VC injection turns to favor enhancing this transition pathway, leading to a reduction of the  $a_\pm$ -state population and therefore weakening the dissociative pathway. Next, using the "VC" result as a reference, we examine the impact of the VEC injection on

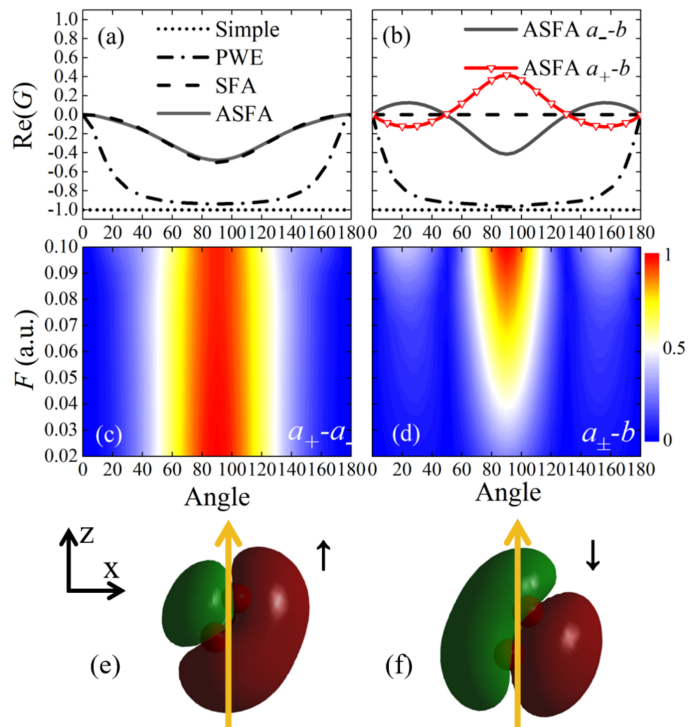


FIG. 4. (Color online) (a), (b) Real components of the complex degree of coherence (DOC) for  $a_- - a_+$  and  $a_\pm - b$  at  $F = 0.09$  a.u. (c), (d) Field-strength-dependent DOC for  $a_- - a_+$  and  $a_\pm - b$ , respectively. (e), (f) Distorted  $1\pi_{ux} \uparrow$  and  $1\pi_{ux} \downarrow$  orbitals at  $F = 0.09$  a.u. and  $\beta = 30^\circ$ ,  $\beta$  is the angle between the molecular axis and the space-fixed  $z$  direction.

the outcomes presented in Fig. 5(b). All models predict a reduction in the dissociation probability (lines with symbols). The primary reason can be attributed to the introduction of the  $a_+ - a_-$  coherence. One can interpret  $a_+ - a_- - b$  within the frame of the  $\Lambda$ -type three-state model described by Eq. (16). The  $a_+ - a_-$  coherence leads to an interference enhancement of the  $a_+ \rightarrow b$  and  $a_- \rightarrow b$  paths. The more robust the  $a_+ - a_-$  DOC, the more pronounced the reduction in  $O_2^+$  dissociation (see Fig. 4(a) for the DOC). For example, the simple model produces the lowest dissociation signals.

Figure 5(b) presents the KER spectrum at  $\beta = 70^\circ$ . When the VC injection is included, apart from a decrease in the dissociation probability, the KER spectrum exhibits distinct peak structures, corresponding to the projection of  $\chi_{v>10}^a$  onto the dissociative states. Upon introducing the VEC injection (solid line with upside-down triangles), the KER spectrum exhibits only a slight decrease, with no significant alteration in its structural characteristics. These peak structures align well with the results of the single-pulse experiment or the IR-pump-IR-probe experiment [44, 48]. Both experiments collect signals perpendicular to the field polarization. To note, these peak structures only appear when the laser pulse is sufficiently long, ensuring that the laser bandwidth is



narrower than the energy spacing between adjacent vibrational levels. At the very least, the agreement between the experimental and the coherence-model results suggest the necessity of considering VC injection in theoretical calculations.

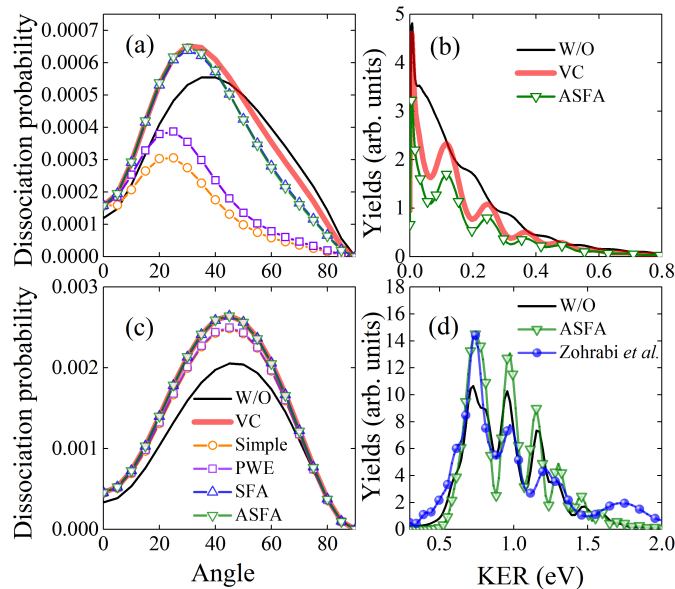


FIG. 5. (Color online) (a) Dissociation probabilities as a function of angle calculated by different models. A 800-nm linearly polarized laser pulse with an intensity of  $1.5 \times 10^{14}$  W/cm<sup>2</sup> is used in the calculation. “W/O” represents the results calculated without considering any coherence injection. “VC” represents the results calculated solely with consideration of the vibrational coherence. (b) Kinetic-energy-release spectra at  $\beta = 70^\circ$ . (c), (d) Same as (a) and (b), but at a wavelength of 400 nm. The solid line with sphere represents the experimental result given in Ref. [48].

The coherence injection amplifies the competition between the pathways of  $a_{\pm} \leftrightarrow b$  and  $a_{\pm} \rightarrow f$ . To reduce the influences of the  $a_{\pm} \leftrightarrow b$  transition, we adjust the laser wavelength to 400 nm. In this case, the TDM between  $\chi_v^a$  and the one-photon resonant  $\chi_v^b$  becomes notably small. In Fig. 5(c), the angle-dependent dissociation probabilities for the 400-nm case are displayed. It is evident that the VC injection now predominantly enhances the  $a_{\pm} \rightarrow f_{\pm}$  transitions, leading to an enhancement in the dissociation signals at almost all angles. Regarding the effect of the VEC injection, only the results for the simple and PWE models exhibit slight decreases in dissociation signals. This is because the  $a_+ - a_-$  DOC is large enough, and its injection still weakly enhances the transition from  $a_{\pm}$  to  $b$ . Figure 5(d) displays the KER spectra in the case of 400 nm at  $\beta = 70^\circ$ . With coherence injection, the KER peaks becomes stronger and sharper. For comparison, we also include experimental results from Ref. [48] obtained by laser-induced dissociation of preprepared O<sub>2</sub><sup>+</sup> beam targets. Unfortunately, whether the coherent injection is considered or not, both results align qualitatively

with the experimental data. This makes it challenging to determine the effectiveness of coherent injection, particularly the VEC injection.

In Fig. 5(a), different coherence models display different angles associated with the maximum dissociation probability. This difference helps determine which model is more reasonable. In addition, our previous work introduced a pump-probe reconstruction scheme to retrieve the molecular DM elements from experimental measurements [49]. By comparing the reconstructed results with model predictions, one can also test the validity of the coherence injection model. However, the above approaches impose strict calibration requirements on the laser intensity. While achievable, it can still be challenging in experiments. Another way to validate the model is by scanning laser parameters and comparing theoretical calculations with experimental results. Here, we performed a laser intensity scan. Figure 6 shows the angle-dependent normalized dissociation probabilities with increasing laser intensities. The laser parameters are set at 800-nm wavelength and 10-fs pulse duration. Such short pulse is utilized to weaken the dipole coupling effects, therefore highlighting the role of the coherence injection. The three models exhibit different slopes for the angles with the maximum values against intensities. These phenomena can be analyzed using Eq. (16). In the PWE model, the ionization-induced  $a_+ - a_-$  coherence is the strongest, as shown in Fig. 4, causing the enhancement of the  $a_{\pm} \rightarrow b$  transition at large angles. Therefore, the signal peak shifts toward smaller angles with increasing laser intensity. In the ASFA model, where the ionization-induced  $a_+ - a_-$  coherence is weaker, the maximum signal angle changes less with increasing intensity. When there is no coherence injection, the peak angle barely changes with intensity. In experiments, the laser intensity can be adjusted by using a variable attenuator [50]. By calibrating the slope of the maximum signal angle against laser intensity, this scanning approach provides a potential way to check the validity of the coherence models.

#### IV. CONCLUSION

In summary, we propose an ASFA coherence injection model based on adiabatic distorted orbitals. This model is utilized to simulate the ultrafast dynamics of molecular ions following the strong-field ionization. We first review previous coherence models, including the simple model and the PWE model. A comparative study reveals that these different models yield consistent trends of the coherence phase, mutually validating the physical rationality of these models. Overall, the simple model predicts the highest instantaneous DOC, followed by the PWE model, the ASFA model, and finally the SFA model. As the field intensity increases, the electronic DOC generated by the ASFA model gradually strengthens. This phenomenon aligns with the transition in the ionization mechanism from the multiphoton regime to the tunnelling regime.

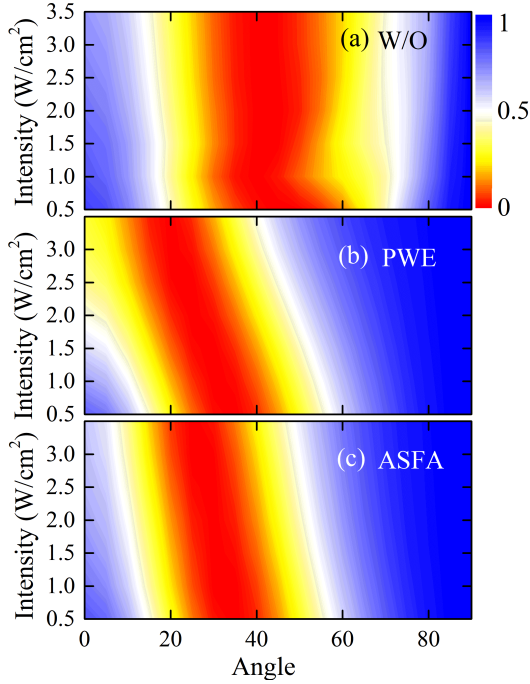


FIG. 6. (Color online) The normalized angle-dependent dissociation probabilities with increasing laser intensities calculated (a) without coherence injection, (b) by the PWE coherence model, and (c) by the ASFA coherence model, respectively.

We also study the effects of the VC and VEC injections on molecular dynamics. The VC injection generally enhances the original transition strength between electronic states. On the other hand, the effect of VEC injection primarily depends on the relative values of the vibronic-state energy difference  $\omega_{vv'}^{ij}$ , and the laser frequency  $\omega$ . For  $N_2$ , the VC injection leads to an enhancement of the  $\chi_{0(1)}^X - \chi_0^B$  population inversion in  $N_2^+$ , while the VEC injection weakens the inversion. This indicates the importance of considering coherence injections in theoretical studies of the  $N_2^+$  lasing process. The control of coherence injection holds the promise of providing new methods for manipulating air lasing. Similar effects are observed in the dissociative ionization dynamics of  $O_2$ . By tuning the laser frequency away from the resonant coupling region of  $a_{\pm} - b$  in  $O_2^+$ , one can minimize the influence of VEC injection. Strong VC injection increases the dissociation probability by over 20%. Illustrated on  $O_2$ , we propose a potential scanning approach to test the validities of different coherence models.

Essentially, ionization-induced coherence is a direct consequence of directional strong-field ionization, akin to injecting an instantaneous electric dipole into the ionized system. This dipole's influence on subsequent ionic dynamics is inevitable due to Coulomb forces. We look forward to experimental validation of our theoretical findings in the near future.

## ACKNOWLEDGEMENT

This work was supported by the National Natural Science Foundation of China (Grants No. 12274188, No. 12004147, No. 12204209), the Natural Science Foundation of Gansu Province (Grant No. 23JRRA1090), and the Fundamental Research Funds for the Central Universities (Grant No. lzujbky-2023-ey08).

## APPENDIX: ORBITAL ANALYSIS OF THE COMPLEX-DOC PHASE IN $N_2^+$ UPON STRONG-FIELD IONIZATION

In the ASFA coherence model, the symmetry of the ionization MO is disrupted due to field distortion. Remembering  $\mathbf{u}_i(\mathbf{p}) \sim -\int \varphi_i \mathbf{r} e^{-i\mathbf{p}\cdot\mathbf{r}} d\mathbf{r}$ ,  $\mathbf{u}_i(\mathbf{p})$  is no longer purely real or imaginary. As a result, coherences arise among all ionic states. Taking the ionization-induced  $X-B$  coherence in  $N_2^+$  as an example, we analyse how the instantaneous coherence is generated in the ASFA model in a dissected manner. Figures 7(a)-7(d) show the adiabatic distorted HOMO ( $3\sigma_g$ ) and HOMO-2 ( $2\sigma_u$ ) orbitals of  $N_2$  at  $\beta = 30^\circ$  and  $F = \pm 0.08$  a.u. One can observe that the MOs tend to be distorted in the opposite direction of the electric field. Figures 7(e)-7(h) display the corresponding dipole interacting terms  $c_i(\mathbf{p}) = \mathbf{u}_i(\mathbf{p}) \cdot \mathbf{F}$ , representing the ionization amplitude of an electron with the momentum  $\mathbf{p}$ . For better comprehension,  $\mathbf{p}$  is confined to the  $xz$ -plane. It is evident that ionization amplitude is more significant along the field polarization. The ionization-induced differential coherence is defined as  $\rho_{XB}^{\text{diff}}(\mathbf{p}) = c_X(\mathbf{p})c_B^*(\mathbf{p})$ . Integrating  $\rho_{XB}^{\text{diff}}(\mathbf{p})$  over  $\mathbf{p}$  yields the final coherence  $\rho_{XB}^{\text{ins}}$ . In Figs. 7(i)-7(l), we display the real and imaginary part of  $\rho_{XB}^{\text{diff}}$ . The imaginary part will cancel out after integration over  $\mathbf{p}$ . One can see that the real components of  $\rho_{XB}^{\text{diff}}$  are negative for  $F > 0$  and positive for  $F < 0$ . The reason is attributed to the inversion relation between the MOs generated by the positive and negative fields, i.e.,

$$\begin{aligned} 3\sigma_g(\mathbf{r}; F > 0) &= 3\sigma_g(-\mathbf{r}; F < 0) \\ 2\sigma_u(\mathbf{r}; F > 0) &= -2\sigma_u(-\mathbf{r}; F < 0). \end{aligned}$$

Therefore

$$\begin{aligned} c_X(\mathbf{p}; F > 0) &= c_X(-\mathbf{p}; F < 0) \\ c_B(\mathbf{p}; F > 0) &= -c_B(-\mathbf{p}; F < 0). \end{aligned}$$

These relations of the ionization amplitude are reflected in Figs. 7(e-h). Due to  $c_{X(B)}(\mathbf{p}) = c_{X(B)}^*(-\mathbf{p})$ , one arrives at  $\rho_{XB}^{\text{diff}}(\mathbf{p}) = -\rho_{XB}^{\text{diff}}(\mathbf{p})$ . Consequently, the integrated coherence changes sign as the field reverses direction as shown in Fig. 1(b).

It's worth noting that the  $3\sigma_g$  orbital exhibits a counterintuitive distortion, with a portion of the red part of the wavepacket twisting along the field direction. This effect intensifies as  $\beta$  approaches  $90^\circ$ . The anomalous

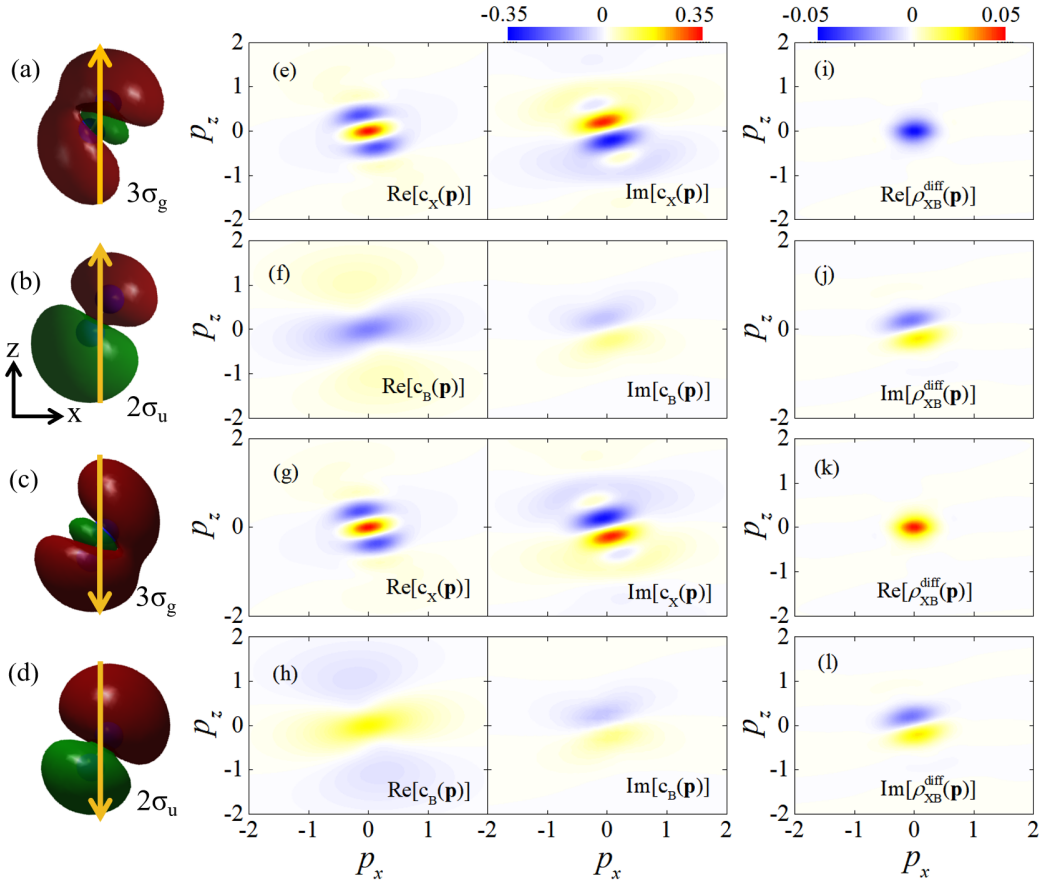


FIG. 7. (Color online) (a), (b) The N<sub>2</sub> distorted molecular orbitals of  $3\sigma_g$  (HOMO) and  $2\sigma_u$  (HOMO-2) at  $F = 0.08$  a.u. and  $\beta = 30^\circ$ . (c), (d) Same as (a) and (b), but at  $F = -0.08$  a.u. (e)-(h) Real and imaginary part of the ionization amplitude  $c_i(\mathbf{p})$  for the orbitals shown in (a)-(d). (i), (j) Real and imaginary part of the differential coherence  $\rho_{XB}^{\text{diff}}(\mathbf{p})$  at  $F = 0.08$  a.u. (k), (l) Same as (i) and (j) but for  $F = -0.08$  a.u.

distortion, likely arising from multi-orbital effects in the self-consistent field calculation, leads to the dip observed

in the ASFA model between  $60^\circ$  and  $120^\circ$ , as shown in Fig. 1(a).

- 
- [1] E. Goulielmakis, Z. Loh, A. Wirth, R. Santra, N. Rohringer, V. S. Yakovlev, S. Zherebtsov, T. Pfeifer, A. M. Azzeer, M. F. Kling, S. R. Leone, and F. Krausz, *Nature* **466**, 739 (2010).
- [2] A. Wirth, M. T. Hassan, I. Grguraš, J. Gagnon, A. Moulet, T. T. Luu, S. Pabst, R. Santra, Z. A. Alahmed, A. M. Azzeer, V. S. Yakovlev, V. Pervak, F. Krausz, and E. Goulielmakis, *Science* **334**, 195 (2011).
- [3] P. M. Kraus, S. B. Zhang, A. Gijsbertsen, R. R. Lucchese, N. Rohringer, and H. J. Wörner, *Phys. Rev. Lett.* **111**, 243005 (2013).
- [4] F. Calegari, D. Ayuso, A. Trabatttoni, L. Belshaw, S. De Camillis, S. Anumula, F. Frassetto, L. Poletto, A. Palacios, P. Decleva, J. B. Greenwood, F. Martín, and M. Nisoli, *Science* **346**, 336 (2014).
- [5] J. Breidbach and L. S. Cederbaum, *J. Chem. Phys.* **118**, 3983 (2003).
- [6] J. Breidbach and L. S. Cederbaum, *Phys. Rev. Lett.* **94**, 033901 (2005).
- [7] L. Belshaw, F. Calegari, M. J. Duffy, A. Trabatttoni, L. Poletto, M. Nisoli, and J. B. Greenwood, *J. Phys. Chem. Lett.* **3**, 3751 (2012).
- [8] H. Hennig, J. Breidbach, and L. S. Cederbaum, *J. Phys. Chem. A* **109**, 409 (2005).
- [9] H. J. Wörner, C. A. Arrell, N. Banerji, A. Cannizzo, M. Chergui, A. K. Das, P. Hamm, U. Keller, P. M. Kraus, E. Liberatore, P. Lopez-Tarifa, M. Lucchini, M. Meuwly, C. Milne, J. E. Moser, U. Rothlisberger, G. Smolentsev, J. Teuscher, J. A. van Bokhoven, and O. Wenger, *Struct. Dynam.* **4**, 061508 (2017).
- [10] A. Palacios, H. Bachau, and F. Martín, *Phys. Rev. Lett.* **96**, 143001 (2006).
- [11] K. L. Ishikawa and T. Sato, *IEEE J. Sel. Top. Quant.* **21**, 1 (2015).
- [12] M. Vacher, M. J. Bearpark, M. A. Robb, and J. P. Malhado, *Phys. Rev. Lett.* **118**, 083001 (2017).

- [13] Q. Zhang, H. Xie, G. Li, X. Wang, H. Lei, J. Zhao, Z. Chen, J. Yao, Y. Cheng, and Z. Zhao, *Commun. Phys.* **3**, 50 (2020).
- [14] H. Lei, J. Yao, J. Zhao, H. Xie, F. Zhang, H. Zhang, N. Zhang, G. Li, Q. Zhang, X. Wang, *et al.*, *Nat. Commun.* **13**, 4080 (2022).
- [15] C. H. Yuen and C. D. Lin, *Phys. Rev. A* **106**, 023120 (2022).
- [16] C. H. Yuen, P. Modak, Y. Song, S.-F. Zhao, and C. D. Lin, *Phys. Rev. A* **107**, 013112 (2023).
- [17] N. Rohringer and R. Santra, *Phys. Rev. A* **79**, 053402 (2009).
- [18] S. Pabst, L. Greenman, P. J. Ho, D. A. Mazziotti, and R. Santra, *Phys. Rev. Lett.* **106**, 053003 (2011).
- [19] S. Pabst, M. Lein, and H. J. Wörner, *Phys. Rev. A* **93**, 023412 (2016).
- [20] S. Carlström, J. Mauritsson, K. J. Schafer, A. L’Huillier, and M. Gisselbrecht, *J. Phys. B: At. Mol. Opt.* **51**, 015201 (2017).
- [21] M. Vacher, L. Steinberg, A. J. Jenkins, M. J. Bearpark, and M. A. Robb, *Phys. Rev. A* **92**, 040502 (2015).
- [22] C. Arnold, O. Vendrell, and R. Santra, *Phys. Rev. A* **95**, 033425 (2017).
- [23] S. Xue, S. Yue, H. Du, B. Hu, and A.-T. Le, *Phys. Rev. A* **104**, 013101 (2021).
- [24] Z. Zhu, S. Xue, Y. Zhang, Y. Zhang, R. Yang, S. Sun, Z. Liu, P. Ding, and B. Hu, *Phys. Rev. A* **108**, 013111 (2023).
- [25] C. H. Yuen and C. D. Lin, *Phys. Rev. A* **108**, 023123 (2023).
- [26] M. D. Śpiewanowski, A. Etches, and L. B. Madsen, *Phys. Rev. A* **87**, 043424 (2013).
- [27] M. D. Śpiewanowski and L. B. Madsen, *Phys. Rev. A* **89**, 043407 (2014).
- [28] M. D. Śpiewanowski and L. B. Madsen, *Phys. Rev. A* **91**, 043406 (2015).
- [29] J. Zhao, J. Liu, X. Wang, J. Yuan, and Z. Zhao, *Chinese Phys. Lett.* **39**, 123201 (2022).
- [30] X.-M. Tong, Z. Zhao, and C.-D. Lin, *Phys. Rev. A* **66**, 033402 (2002).
- [31] S.-F. Zhao, C. Jin, A.-T. Le, T. F. Jiang, and C. D. Lin, *Phys. Rev. A* **81**, 033423 (2010).
- [32] O. I. Tolstikhin, T. Morishita, and L. B. Madsen, *Phys. Rev. A* **84**, 053423 (2011).
- [33] S. Song, M. Zhu, H. Ni, and J. Wu, *Comput. Phys. Commun.* **292**, 108882 (2023).
- [34] M. J. Frisch, G. W. Trucks, and H. B. S. *et al.*, Gaussian 16 Revision C.01, Gaussian Inc. Wallingford CT (2016).
- [35] J. Yao, B. Zeng, H. Xu, G. Li, W. Chu, J. Ni, H. Zhang, S. L. Chin, Y. Cheng, and Z. Xu, *Phys. Rev. A* **84**, 051802 (2011).
- [36] H. Xu, E. Lötstedt, A. Iwasaki, and K. Yamanouchi, *Nat. Commun.* **6**, 8347 (2015).
- [37] Y. Liu, P. Ding, G. Lambert, A. Houard, V. Tikhonchuk, and A. Mysyrowicz, *Phys. Rev. Lett.* **115**, 133203 (2015).
- [38] Y. Liu, P. Ding, N. Ibrakovic, S. Bengtsson, S. Chen, R. Danylo, E. R. Simpson, E. W. Larsen, X. Zhang, Z. Fan, A. Houard, J. Mauritsson, A. L’Huillier, C. L. Arnold, S. Zhuang, V. Tikhonchuk, and A. Mysyrowicz, *Phys. Rev. Lett.* **119**, 203205 (2017).
- [39] M. Britton, P. Laferrière, D. H. Ko, Z. Li, F. Kong, G. Brown, A. Naumov, C. Zhang, L. Arissian, and P. B. Corkum, *Phys. Rev. Lett.* **120**, 133208 (2018).
- [40] C. Kleine, M.-O. Winghart, Z.-Y. Zhang, M. Richter, M. Ekimova, S. Eckert, M. J. J. Vrakking, E. T. J. Nibbering, A. Rouzée, and E. R. Grant, *Phys. Rev. Lett.* **129**, 123002 (2022).
- [41] M. Richter, M. Lytova, F. Morales, S. Haessler, O. Smirnova, M. Spanner, and M. Ivanov, *Optica* **7**, 586 (2020).
- [42] Y. Zhang, E. Lötstedt, and K. Yamanouchi, *Phys. Rev. A* **101**, 053412 (2020).
- [43] Y. Zhang, E. Lötstedt, and K. Yamanouchi, *Phys. Rev. A* **106**, 063109 (2022).
- [44] S. De, M. Magrakvelidze, I. A. Bocharova, D. Ray, W. Cao, I. Znakovskaya, H. Li, Z. Wang, G. Laurent, U. Thumm, M. F. Kling, I. V. Litvinyuk, I. Ben-Itzhak, and C. L. Cocke, *Phys. Rev. A* **84**, 043410 (2011).
- [45] M. Magrakvelidze, C. M. Aikens, and U. Thumm, *Phys. Rev. A* **86**, 023402 (2012).
- [46] P. Cörlin, A. Fischer, M. Schönwald, A. Sperl, T. Mizuno, U. Thumm, T. Pfeifer, and R. Moshhammer, *Phys. Rev. A* **91**, 043415 (2015).
- [47] S. Xue, H. Du, B. Hu, C. Lin, and A.-T. Le, *Phys. Rev. A* **97**, 043409 (2018).
- [48] M. Zohrabi, J. McKenna, B. Gaire, N. G. Johnson, K. D. Carnes, S. De, I. A. Bocharova, M. Magrakvelidze, D. Ray, I. V. Litvinyuk, C. L. Cocke, and I. Ben-Itzhak, *Phys. Rev. A* **83**, 053405 (2011).
- [49] S. Xue, S. Sun, P. Ding, B. Hu, S. Yue, and H. Du, *Phys. Rev. A* **105**, 043108 (2022).
- [50] P. Ding, M. Ruchkina, Y. Liu, M. Alden, and J. Bood, *Opt. Lett.* **43**, 1183 (2018).